

Full Length Article

Photopolymer formulation to minimize feature size, surface roughness, and stair-stepping in digital light processing-based three-dimensional printing

Kavin Kowsari^a, Biao Zhang^a, Sahil Panjwani^a, Zaichun Chen^b, Hardik Hingorani^a, Saeed Akbari^a, Nicholas X. Fang^c, Qi Ge^{a,b,*}

^a Digital Manufacturing and Design Center, Singapore University of Technology and Design (SUTD), Singapore, 487372, Singapore

^b Science and Math Cluster, Singapore University of Technology and Design (SUTD), Singapore, 487372, Singapore

^c Department of Mechanical Engineering, Massachusetts Institute of Technology (MIT), Cambridge, MA 02139, USA

ARTICLE INFO

Keywords:

Three-dimensional (3D) printing
Digital light processing (DLP)
Printing resolution
Photopolymer formulation

ABSTRACT

Achievement of optimized lateral and vertical resolution is a key factor to obtaining three-dimensional (3D) structural details fabricated through digital light processing (DLP)-based 3D printing technologies which exploit digitalized ultraviolet (UV) or near-UV light to trigger localized photopolymerization forming solid patterns from liquid polymer resins. Many efforts have been made to optimize printing resolution through improving the optical systems. However, researchers have paid comparatively little attention to understand the influences of polymer formulation on the printing resolution and surface quality. Here, we report an investigation on the effects of in-house formulated (meth)acrylate-based photopolymer constituent types and concentrations on the resolution and quality of structures printed on a bottom-exposure DLP-based 3D printing system. We examined a wide variety of resin formulations to determine optimal formulations that yield best printing resolution and surface quality over a reasonably broad range of mechanical properties. We demonstrated the controlled fabrication of sub-pixel conical and aspherical smooth features, whereby the shape and dimensions could be prescribed with the resin formulation and process parameters. Such features hold promising implications in micro-optic and microfluidic fabrication using the DLP-based 3D printing technique. Additionally, we devised di(meth)acrylate-based resin formulations which could exclusively produce optically-clear layers in contrast to opaque, rough surfaces resulting from commonly-used diacrylate-based resins including those available commercially. Use of this solution minimized the 'stair-stepping' effect in components printed in a layer-by-layer manner. We also showed that the maximum lateral and vertical resolution attainable using our present system were 7 μm and 4 μm , respectively, while maintaining uniform width and height. Taken together, the present findings provide a basis for optimized photopolymer resin formulations that retain maximum vertical and lateral resolutions and minimal surface roughness and layering artifacts for a versatile range of mechanical and rheological properties suited to novel applications in 3D printing of smooth free-form solids, micro-optics, and direct fabrication of microfluidic platforms with functional surfaces.

1. Introduction

Three-dimensional (3D) printing encompasses and integrates chemistry and engineering, thereby enables precise fabrication of complex microarchitectures with novel functionalities and optimized performance made of a variety of materials [1–4]. Much of the scientific applications demand components with micron-scale features, where digital light processing (DLP)-based 3D printing, amongst other complementary techniques such as fused deposition modeling (FDM), Polyjet, selective laser sintering (SLS), direct ink writing (DIW), and laser stereolithography (SLA), finds viable applications as an

inexpensive, quick, and efficient (minimal material waste) process [5–8]. In addition, the DLP-based 3D printing is compatible with virtually any custom-formulated photocurable resins and often does not require the use of support materials to print hollow or porous components [5,6,8–10]. In DLP-based 3D printing, the projected ultraviolet (UV) or near-UV patterns trigger localized free-radical photopolymerization which transforms liquid photopolymer precursors into solid 3D objects. During photopolymerization, the low molecular weight monomers and oligomers in liquid photopolymer precursor connect with each other to form large molecular weight solid networks. Recent notable advances in microfabrication by photopolymerization

* Corresponding author.

E-mail address: ge_qi@sutd.edu.sg (Q. Ge).

<https://doi.org/10.1016/j.addma.2018.10.037>

Received 10 July 2018; Received in revised form 21 October 2018; Accepted 21 October 2018

Available online 28 October 2018

2214-8604/ © 2018 Elsevier B.V. All rights reserved.

include sub-micron printing resolution in multiscale (nano-meso) lattice metamaterials [7], single-step, rapid volumetric fabrication using holographic patterning of light fields [11], continuous liquid interface production (CLIP) with about 100-fold faster printing [12], biomimetic super-hydrophobic functional surfaces [13], microfluidic device fabrication [14], as well as multimaterial capability to produce heterogeneous structures suited for a wide array of engineering and biological technological applications [6,15–18].

Despite the high resolution (up to 0.6 μm [8]) afforded by projection microstereolithography (P μ SL) [6–8,12,16,19–23], this method has also imposed its own new set of fabrication constraints. Namely, the quality of printed components is limited by a stair-stepping phenomenon owing to the layer-by-layer production [24,25]. More importantly, surface topography of printed layers is highly-sensitive to the light intensity distribution along layer cross-sections, inherently caused by minute ‘dead’ spaces between micro-mirror arrays present in images produced by digital micromirror devices (DMD) [25]. Another drawback is the conflict between build size (projection field-of-view) and resolution (pixel size) imposed by the size of currently-available DMD devices, which has been overcome using dynamically-scanning optics or stitched projection [7,20,21,26,27]. Furthermore, formulation design of photopolymer constituents is essential for the performance and properties of photopolymerization-based 3D printing systems [28]. Several studies [8,14,28–31] attempted to formulate resins suited for P μ SL [14], which generally found that the use of photoabsorbers, or the chemical structures thereof, improved lateral and vertical printing resolution as the additives yield greater control of light scattering and penetration [14,32,33]. Within the bottom-exposure DLP-based 3D printing paradigm, existing studies either used commercially-available resins [19,34], or customized photocurable polymers [9,35]. In both cases, the authors mostly aimed to establish the relationship between prepolymer composition and mechanical properties, thereby overlooked the comparative effects of resin formulation on printing characteristics such as edge definition (i.e. resolution), edge slope, and surface quality. In this regard, there is a need to establish the relationship between commonly-employed photopolymer constituents and the resulting resolution and quality over a range of mechanical properties.

In summary, optimizing lateral and vertical resolution can facilitate precise 3D printing of structures containing micro- and even sub-microscale features. However, the effects of optimization do not only rely on the optical resolution of 3D printer but also on the formulation of photopolymer used in 3D printing and the processing parameters. Herein, in this paper, we report, for the first time, an investigation on the effects of custom formulated mono-, di-, and tri-functional (meth)acrylate-based photopolymer constituent types and concentrations on the shape evolution, size, resolution, and surface roughness of features made using single- and multi-pixel DLP projections. We then demonstrate the implications of the novel findings that enable the fabrication of optically-clear surfaces with minimized ‘stair-stepping’ effect and maximized resolution using DLP-based 3D printing.

2. DLP-based 3D printing system and materials

Two types of experiments were performed as summarized in Fig. 1: (i) micro-structure fabrication (Fig. 1a), and (ii) single-exposure (i.e. single-layer) tests for resolution assessment (Fig. 1b). The DLP-based 3D printing system used as the basis for this work in the experiments is described in full detail in Kowsari et al. (2018) [25]. Though the system is capable of multimaterial fabrication [25], the present work focusses on resolution assessment of various materials separately, where the implications of findings can be extended for use in multimaterial fabrication. Briefly, liquid photocurable resins are subjected to 405 nm image projections through a 5 mm-thick borosilicate glass plate (Borofloat 33, Schott AG, Mainz, Germany), covered with optically-clear PTFE FEP (CS Hyde, Lake Villa, IL, USA), which facilitates the separation of the printed layers from the glass plate, shown in the close-up

illustration of Fig. 1c. The electronic components of the apparatus are controlled in sequence using codes written in LabVIEW 2016 (National Instruments, Austin, TX, USA). Three-dimensional computer-aided design (CAD) structures are sliced into a series of 2D images with a prescribed layer thickness, which are then transmitted to a DLP-based projector (CEL5500, Digital Light Innovations, Austin, TX, USA) which irradiates the modulated 405 nm light with the corresponding 2D image for each layer onto the surface of polymer resin using millions of individually-controlled moving micromirrors. For the printing experiments, a paired achromatic doublet lens was used to reproduce the digital micromirror device chip at the focal plane with a ratio of approximately 1:1 corresponding to image pixel width of about 7 μm .

As will be shown in Section 3.2, the characteristics of patterned single-layer features were produced using the setup in Fig. 1b, in which customized near-UV image projections containing single pixels, lines, and surfaces were focused at the liquid-glass interface of a 200 μm -thick cover slip submerged within the liquid photopolymer bath for various controlled-exposure durations. As depicted in Fig. 1f, liquid puddles were maintained to a much higher height than the fabricated features to prevent any oxygen inhibition. Single-pixel characterization was performed using larger pixels (i.e. about 50 μm) so that geometries of sub-pixel solid formations could be captured and closely-examined at a sufficiently high image quality as the process is scalable over the 7–50 μm pixel range in this study. The light intensity of the DLP was maintained at an intensity of about 120 lumens corresponding to 400 mW at a wavelength of 405 nm as provided by the manufacturer. Upon completion of each exposure, cover slips containing solid patterns were submerged in a water bath for approximately 15 s to rinse any uncured resin, gently blasted with air, then dried in ambient air for 30 min. The solid patterns were then gold-sputtered and viewed for analysis in a field emission scanning electron microscope (FESEM) (JSM-7600 F, Jeol Ltd., Tokyo, Japan).

Photopolymer precursors are prepared by mixing monomers and oligomers, photoinitiators and other additives. During 3D printing, the patterned near-UV image projection for each layer triggers photopolymerization which connects monomers and oligomers to form macromolecules, and transfers liquid solution into a corresponding patterned solid material. The photoinitiator cleaves upon irradiation to connect monomers and oligomers that constitute the backbone of the 3D polymer network. The photopolymer precursor absorbs light where its photoinitiator system converts photolytic energy into reactive species to induce polymerization. In general, free-radical polymerization occurs over the following steps: (i) initiation, where radicals formed by the photoinitiator attack monomers/oligomers; (ii) propagation, during which radicals attack other monomers/oligomers to produce chain growth and crosslinking; and (iii) termination, when two radicals meet each other to stop the polymerization [36]. Two important stages are described as gelation and vitrification [37]. The gelation stage, a kinetic effect, is characterized by the formation of a highly-crosslinked polymer network leading to a significant increase in viscosity, corresponding to a rubbery state. Two phases coexist in this stage, namely a non-soluble solid phase and a less-reacted soluble liquid phase. Beyond a viscosity and crosslinking threshold, the polymer reaches the physical vitrification stage, transforming into a glassy state. Diffusion of free monomers/oligomers stops due to the limited liquid phase amount [38].

(Meth)acrylate-based photopolymers have been widely-utilized for DLP-based 3D printing given their high penetration depth, high mechanical property tailorability, and reasonable cost. We selected the following (meth)acrylate-based monomers/oligomers involving single- and multi-functional reactive groups: 2-Hydroxyethyl acrylate (HEA), poly(propylene glycol) acrylate (PPGA), 1,6-Hexanediol diacrylate (HDDA), poly(ethylene glycol) diacrylate (PEGDA), 1,6-Hexanediol di(meth)acrylate (HDDMA), trimethylolpropane ethoxylate triacrylate (TETA).

Useful photoinitiator systems must conform to basic requirements such as thermal stability and strong absorption in the wavelength

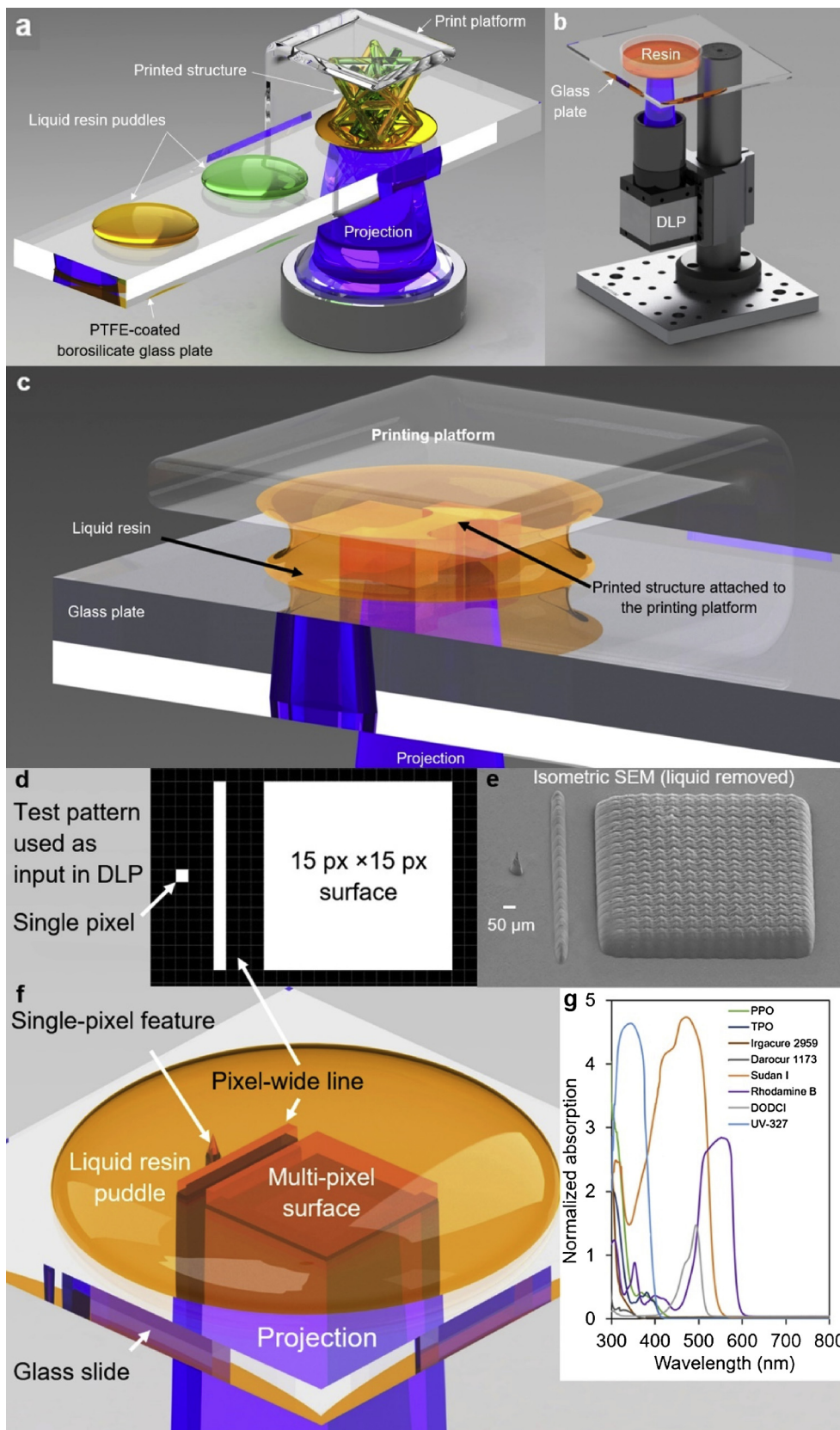


Fig. 1. Labeled illustrations of the multimaterial DLP-based 3D printing system. Configurations used for (a) structure fabrication, and (b) resolution assessment. (c) Close-up of the printed structure within liquid resin during printing. (d) Test patterns used as input in the DLP. (e) Single pixels, single-pixel wide lines, and multi-pixel micro-features formed upon polymerization. (f) Printing configuration to produce the features in (e). (g) Normalized absorption vs irradiance wavelength obtained using ultraviolet-visible spectrometry.

region of interest to efficiently generate reactive species upon irradiation to attack monomers/oligomers and initiate polymerization. In this study, we select four commonly used photoinitiators including phenylbis(2,4,6-trimethylbenzoyl)phosphine oxide (PPO/Irgacure 819), diphenyl(2,4,6-trimethylbenzoyl)phosphine oxide (TPO), 1-[4-(2-Hydroxyethoxy)-phenyl]-2-hydroxy-2-methyl-1-propane-1-one (Irgacure 2959), 2-Hydroxy-2-methylpropiophenone (Darocur 1173). Fig. 1g displays the linear absorption spectrum for the initiators and absorbers used in this work, obtained using a UV/VIS/NIR spectrometer (Lambda 750 S, PerkinElmer Inc., Waltham, MA, USA) with a sampling interval of 1 nm and ethanol as the primary solvent. The plot shows that TPO and PPO initiators, as well as Sudan I and Rhodamine B absorbers were reasonable selections due to their large absorbance in the 300–450 nm range. As will be shown in Section 3.2.1, relatively high concentrations of photoinitiators were needed to trigger photopolymerization for practical curing depths. This is explained by the lower absorbance of the aforementioned photoinitiators at larger wavelengths such as that used in the present work (405 nm), which lies in the visible light range, comparative to typical UV sources used in DLP-based 3D printing systems (e.g. 364 nm) [8]. Therefore, this necessitated relatively large photoinitiator concentrations. Irgacure 2959 and Darocur 1179 initiators along with DODCI and UV-327 absorber exhibited peak absorbance around 500 nm and 350 nm, respectively, thereby were relatively unresponsive to the 405 nm light source, thus were not used in the solutions listed in Table 1.

Moreover, use of a photoabsorber can have a profound effect on the light penetration and printed resolution [14,32,33]. The photoabsorbers used in study include $C_{16}H_{12}N_2O$ (Sudan I), $C_{28}H_{31}ClN_2O_3$ (Rhodamine B), 3,3'-Diethyloxycarbocyanine iodide (DODCI), 2-tert-Butyl-6-(5-chloro-2H-benzotriazol-2-yl)-4-methylphenol (UV-327). Alongside in-house formulated photopolymer precursors described above purchased from Sigma-Aldrich (Sigma-Aldrich Corp., St. Louis, MO, USA), a commercially-available acrylate-based resin, 3DM-ABS

(3DM, Dublin, CA, USA), was used for the initial light characterization experiments of Section 3.1.

Table 1 summarizes the types and concentrations of the constituents used in the study and also provides rheological visual properties of the formulated resins. The appearance as described was inspected visually. Fluid viscosities were measured using a hybrid rheometer (Discovery HR-2, TA Instruments, New Castle, DE, USA) using a 40 mm flat tip over a 50 mm Peltier plate.

3. Results and discussions

To characterize resolution, we print principal features corresponding to the test pattern shown in Fig. 1d. Most fundamentally, solid formations due to single-pixel irradiation was investigated, since, any arbitrary pattern is constituted of individual adjacent pixels. Pixel-wide lines and multi-pixel surfaces (15 pixel \times 15 pixel) were also tested as illustrated in the SEM micrographs of Fig. 1d. Image projections of these model geometries were focused on the flat glass surface to form relatively thin features on the surface within a liquid resin puddle resting on the glass. In these trials, the exposure time was incrementally increased to quantitatively capture and analyze the shape evolution of the solid features.

3.1. Optical field and surface evolution characterization

Uniformity of light intensity distribution is a crucial parameter for precise formation of 3D solid features, where the shape, size, and surface texture of cured layers highly correspond to the regions within the optical field with sufficient energy to trigger polymerization. In this regard, the vertical curing precision is related to the curing depth, C_d , which is theoretically expressed using Jacob's working curve [39] as

$$C_d = D_p \ln \left(\frac{E_0}{E_c} \right) \quad (1)$$

Table 1

Composition and measured properties of the photocurable precursors used in the experiments. Concentrations are given as wt% of monomer/oligomer.

Sol'n no.	Photopolymer constituent				Rheological and visual properties	
	Monomer/oligomer, $g\text{mol}^{-1}$	Crosslinker, $g\text{mol}^{-1}$, vol. fraction	Initiator, wt%	Absorber, wt%	Liquid viscosity at 25 °C (η , Pa·s)	Liquid appearance
1	HDDA, 226	–	PPO, 2.5	–	1.77E-02	Transparent, slightly green
2	HDDA, 226	–	PPO, 5	–	1.61E-02	Transparent, slightly green
3	HDDA, 226	–	TPO, 5	–	2.06E-02	Transparent, colorless
4	HDDA, 226	–	TPO, 7.5	–	1.86E-02	Transparent, colorless
5	HDDA, 226	–	TPO, 10	–	1.91E-02	Transparent, slightly green
6	PPGA, 475	–	PPO, 2.5	–	1.77E-02	Transparent, slightly green
7	HDDMA, 254	–	PPO, 2.5	–	1.97E-02	Transparent, slightly green
8	TETA, 428	–	PPO, 2.5	–	8.96E-02	Transparent, slightly green
9	PEGDA, 250	–	PPO, 2.5	–	2.38E-02	Transparent, slightly green
10	PEGDA, 575	–	PPO, 2.5	–	7.05E-02	Transparent, slightly green
11	PEGDA, 700	–	PPO, 2.5	–	1.25E-01	Transparent, slightly green
12	HEA, 116	–	PPO, 5	–	1.84E-02	Transparent, slightly green
13	HDDA, 226	–	PPO, 2.5	Sudan I, 0.1	2.20E-02	Transparent, orange
14	HDDA, 226	–	PPO, 5	Sudan I, 0.5	1.97E-02	Transparent, red
15	PPGA, 475	–	PPO, 2.5	Sudan I, 0.1	1.43E-01	Transparent, orange
16	HDDMA, 254	–	PPO, 5	Sudan I, 0.1	2.10E-02	Transparent, orange
17	TETA, 428	–	PPO, 5	Sudan I, 0.1	1.13E-01	Transparent, orange
18	PEGDA, 700	–	PPO, 2.5	Rhod. B, 0.1	1.34E-01	Transparent, pink
19	PEGDA, 700	–	PPO, 2.5	Sudan I, 0.1	1.87E-01	Transparent, orange
20	PEGDA, 700	–	PPO, 2.5	DODCI, 0.1	1.37E-01	Transparent, yellow
21	PPGA, 475	HDDA, 226, 0.5	TPO, 7.5	–	4.41E-02	Transparent, colorless
22	PPGA, 475	HDDMA, 254, 0.5	TPO, 7.5	–	3.44E-02	Transparent, colorless
23	PPGA, 475	TETA, 428, 0.5	TPO, 7.5	–	1.33E-01	Transparent, colorless
24	HDDA, 226	HDDMA, 254, 0.5	TPO, 7.5	–	2.21E-02	Transparent, colorless
25	HDDA, 226	TETA, 428, 0.5	TPO, 7.5	–	2.43E-02	Transparent, colorless
26	HDDMA, 254	TETA, 428, 0.5	TPO, 7.5	–	2.59E-02	Transparent, colorless
27	PPGA, 475	HDDMA, 254, 0.5	TPO, 7.5	Sudan I, 0.1	1.33E-01	Transparent, orange
28	PPGA, 475	TETA, 428, 0.5	TPO, 7.5	Sudan I, 0.1	2.21E-02	Transparent, orange
29	HDDA, 226	HDDMA, 254, 0.5	TPO, 7.5	Sudan I, 0.1	2.43E-02	Transparent, orange
30	HDDMA, 254	TETA, 428, 0.5	TPO, 7.5	Sudan I, 0.1	2.59E-02	Transparent, orange

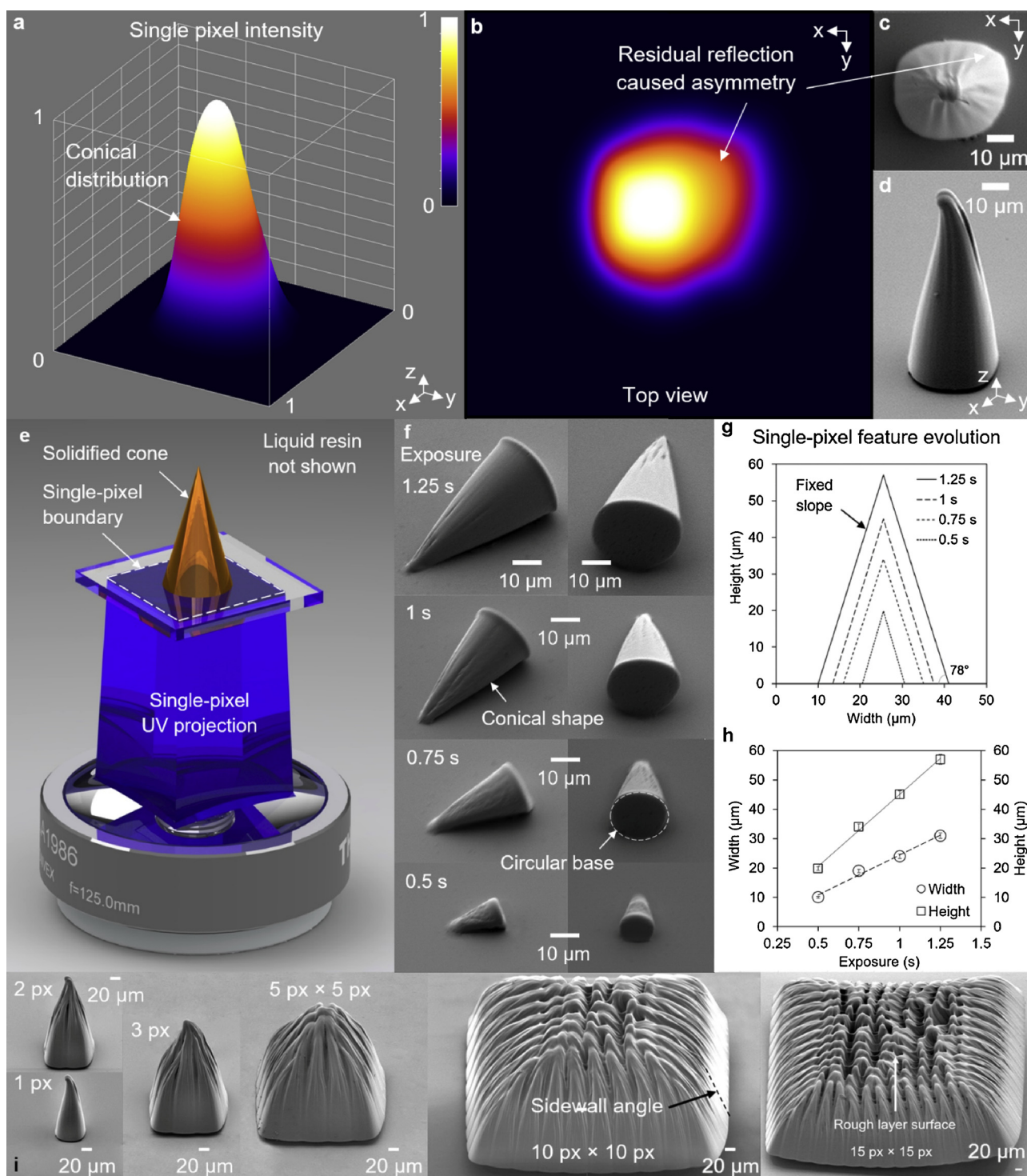


Fig. 2. Light intensity characterization and elemental feature formation. (a) 3D and (b) 2D plots of the planar irradiation intensity distribution captured using a CMOS sensor. (c–f) Top and isometric views of features fabricated using a single-pixel projection as a function of exposure time. (g) Cross-sectional profiles, and (h) dimensions versus exposure of the features in (b). (i) Isometric SEM images of 1 px × 1 px up to 15 px × 15 px features.

Where D_p is the penetration depth (an intrinsic property of a photopolymer precursor), and E_0 and E_c are the irradiation intensity at the surface and critical exposure to induce polymerization, respectively [40].

An arbitrary multi-pixel pattern corresponds to the superposition of adjacent single pixels. The light intensity distribution within the cross-sectional area of a 50 μm pixel, quantified using a 35.9-megapixel CMOS sensor having a pixel width of 4 μm (D810, Nikon Corp. Tokyo, Japan) using the commercial 3DM-ABS resin, shown in Fig. 2a and b,

corresponded to a nearly conical shape; i.e. the light intensity was maximum at the center of the pixel. The top view in Fig. 2b reveals stray light extending from one of the four edges, consistent with the finding of Kowsari et al. (2018) who explained that this directional light was likely caused by the oblique incidence of the light source on a tilted micro-mirror. Fig. 2c and d display top and isometric SEM views of a solidified feature forming due to a single pixel and demonstrate that the obtained geometry was consistent with the light contour plot. The surface evolution of cones protruding due to increasing exposure

duration of a single pixel using the experimental setup of Fig. 2e revealed that circular-based cones progressively enlarged in both height and base diameter with increasing exposure as evident in Fig. 2f. The shapes of these cones, plotted in Fig. 2g, showed that the edge slope remained constant at approximately 78°. Moreover, both the height and base diameters increased linearly as seen in the plot of Fig. 2h. Each measurement was repeated three separate times and the variation in the height or width of a feature produced under identical conditions was less than 3%. It is interesting to note that the 50 µm pixel width was 61% larger than the base diameter of the solidified conical feature for a 1.25 s exposure, which explains the circular, rather than square, shape of the feature's base (Fig. 2f). As the top-view of a single-pixel feature shown in Fig. 2c shows a base shape that corresponds more to a square than a circle, proves that single-pixel shapes evolve by protruding from a circular cone at the central region of a pixel as in Fig. 2g, followed by eventual development into a square-based conical shape when subjected to sufficient exposure. A surface or layer spanning over multiple pixels evolve due to the superposition of conical single-pixel profile as evident in the SEM images of 2–15 pixel-wide square patterns formed using the commercial 3DM-ABS resin in Fig. 2i. It is seen that the produced surfaces were rough due to the discretization of the pattern into multiple surfaces that created non-uniformity in the light intensity distribution across the pattern. However, as will be shown in the following Sections, layer geometry and surface quality also depend on resin constituent type and concentration.

3.2. Photopolymer formulation

The investigational approach that guides the parametric study is driven by the role of each constituent in the photopolymerization reaction. We follow the formulation strategy outlined in Table 1, investigating individual and hybrid monomer/oligomer combinations with various initiators and absorbers.

3.2.1. Effects of photoinitiators and monomer molecular weight

The photoinitiator constituent plays a key role in photopolymerization as it controls the penetration depth of the light, hence can consequently dictate the shape of cured features. As summarized in Table 1, we take advantage of various photoinitiators to identify any changes induced in the geometry of printed features associated with the initiator type. A PPO concentration of 2.5 wt% (solution #1 in Table 1) subjected to exposure times ranging from 0.5 to 90 s produced features with logarithmically-increasing heights (Fig. 3a), and with preferential curing in a randomized direction that caused asymmetry and unevenness in the surfaces (Fig. 3b–e). Referring to Fig. 3a, such working curves are typically presented in semi-logarithmic plots (i.e. logarithmic x-axis and linear y-axis); however, we presented our data in a fully logarithmic manner for optimized visualization of the working curves at lower exposure durations. This 'over-curing' phenomenon seen in single-pixel (Fig. 3b(i)), single-pixel lines (Fig. 3b(ii)), and multi-pixel surfaces (Fig. 3b(iii)), is attributed to over-penetration of irradiation with sufficiently high energy to trigger photopolymerization, and/or influence of dissolved PPO within the HDDA matrix to vary the refraction index to cause an associated self-focusing [41]. Though the phenomenon of photopolymerization-induced refractive index (RI) increase has been experimentally demonstrated [41], we also measured changes in refractive indices of selected solutions using spectrometry (see Appendix for methods). Table 2 summarizes the results and shows that all tested solutions underwent an increase of about 4–6%, on average, in their refractive index upon solidification. The observed changes are consistent with previously-reported findings suggesting that solid surfaces that form in the initial stage of the reaction produce a 'lensing effect' by bending incident photons. These stray beams generated by the solids are known to cause residual curing, which explains the 'top hats' seen in the single-pixel features of Fig. 3bi. The superposition of many adjacent features with such geometry consequently

produces a layer with sharp protrusions extending from each pixel, which produce the rough surfaces seen in Fig. 3biii. Moreover, the surface unevenness caused by residual curing in Fig. 3biii, d, and e are also attributable to the lensing effect. As will be shown in Section 3.2.2, use of a photoabsorber can effectively prevent such residual curing by absorbing the stray light intensity.

Saturation was reached below 7.5 wt% PPO, as reflected in the formation of irregular voids seen in Fig. 3c. Similarly, single-pixel features formed within solutions #3–5 containing the TPO initiator were conical but with a less pronounced irregularity at the tip (Fig. 3c). Moreover, the base diameters and heights of single-pixel cones increased in the logarithmic nature of vat photopolymerization [42]. Fig. 3b and d show that over-curing was seen in surfaces producing severe unevenness while compromising the lateral resolution as the edges of layers began to grow laterally.

Viscosity, i.e. resistance to flow, is a function of molecular weight and chain entanglement and is modulated by polymer architecture such that short polymer chains with fewer chain entanglements attenuate viscosity. Low molecular weight oligomers exhibit increased solubility, and easier processing compared to their long-chained counterparts. The effects of polymer chain length were explored for a given oligomer, PEGDA, whereby M_w was varied between 250, 575, 700 g·mol⁻¹ for solutions containing identical amounts of PPO initiator (Table 1). As in Fig. 3f, 700 g·mol⁻¹ PEGDA displayed the highest curing depth for a given exposure. This is attributable to the initially-long polymer chains requiring less crosslinking to reach sufficiently-high viscosities (i.e. gelation) corresponding to a solid bulk state, whereas short-chained 250 g·mol⁻¹ PEGDA required more chain-linking, and therefore longer, to accomplish. Increasing M_w i) decreased over-curing (Fig. 3g), ii) produced a line with a uniform height (Fig. 3h), iii) and increased liquid viscosity (Fig. 3i).

3.2.2. Effects of monomer/oligomer functional group, photoabsorber, and crosslinker

As described in Section 2, altering the reactive end of oligomeric constituents of (meth)acrylates can influence the reaction kinetics and potentially the solid formation topology. The working plot of Fig. 4a demonstrates that the tri-functional acrylate had the highest curing depth whereas the di(meth)acrylate-based resin was the least reactive amongst all functional group types. In the same way as Fig. 3a, the axes of Fig. 4a were also presented logarithmically for improved clarity of data at low exposures. Variations in curing depth were also accompanied by significant differences in edge slope and surface quality. It should be noted that layer surface topographies were independent of exposure time for the range of thicknesses examined. For instance, the monoacrylate produced surfaces with markedly smoother surfaces and near-vertical edge slopes. Additionally, the single-pixel monoacrylate feature shown in Fig. 4b had a 10% steeper edge than that produced using the same initiator but with diacrylate or triacrylate oligomers. These differences can be explained by changes in refractive index during curing, causing a self-focusing effect in the investigated resins. It should be noted that the refractive indices of all liquid monomers are approximately equal (Table 1) and the refractive index of a solution in its liquid state has no or only minor influence on the self-focusing of the beam [41]. Moreover, mono-, di-, and tri-functional monomers and varying molecular weights would lead to different shrinkage and therefore different change of refractive indices while curing [42]. Of particular interest was the di (meth)acrylate-based solution that produced rounded single-pixel features and optically-clear surfaces (Fig. 4c), the implications of which will be shown in Section 3.3.

Besides reactive groups and initiator types, resin formulations can benefit from contained photoabsorbers or inhibitors to better-control the penetration depth and inherently solve the over-curing issue observed in much of the bare monomer/oligomer-initiator solutions such as those used in the preceding Sections. The addition of a small amount of Sudan I (i) eliminated over-curing (Fig. 4d), (ii) significantly reduced

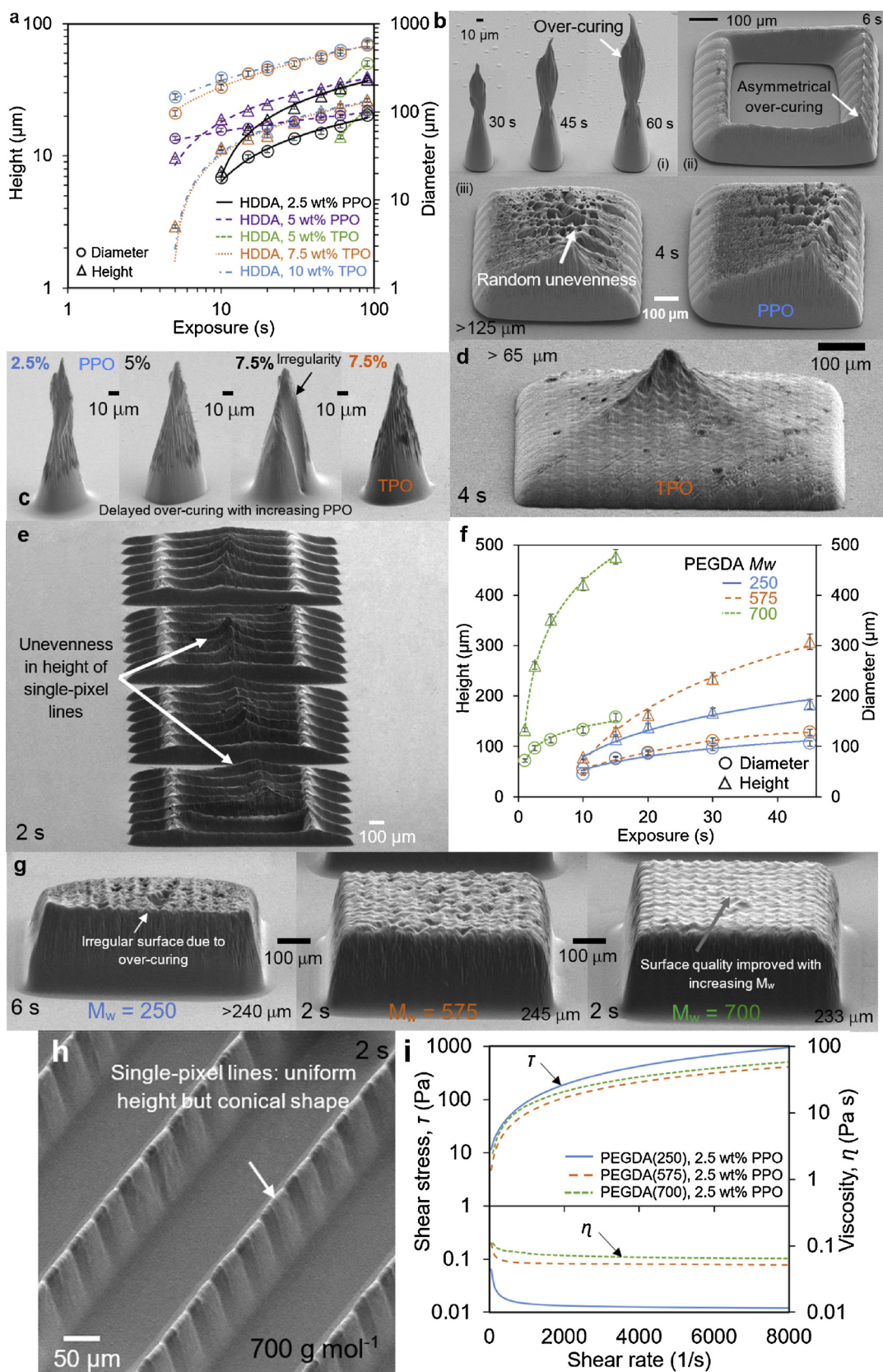


Fig. 3. Effects of monomer molecular weight and photoinitiator (solutions #1-5 and 9–11). Plots of single-pixel feature size versus exposure using (a) HDDA-based and (f) PEGDA-based photopolymers. Isometric SEM views of single-pixel, pixel-wide lines, and 15 px × 15 px surface features for (b–e) HDDA-based and (g–h) PEGDA-based resins. (i) Plot of shear stress and viscosity versus shear rate.

Table 2

Comparison of measured refractive indices (RI) between liquid and solidified states of various photopolymer formulations. The liquid indices were obtained from the manufacturer (<http://sigmaaldrich.com>).

Monomer/oligomer, g mol ⁻¹	RI (liquid)	RI (crosslinked)
HDDA, 226	1.456	1.520
HDDMA, 254	1.458	1.525
PEGDA, 250	1.463	1.545
PEGDA, 575	1.467	1.535
PEGDA, 700	1.47	1.530
TETA, 146	1.471	1.569

surface roughness by transforming the conical single-pixel feature to a dome-shape (Fig. 4e), (iii) reduced the minimum thickness to a minimum of less than 5 μm , (iv) and reduced widening with increasing exposure (Fig. 4d). These attributions are explained by the ability of the absorber to reduce penetration depth (Eq. 1), thereby preventing solidification due to reflected light in regions outside of illuminated pixels. Correspondingly, Fig. 4d also shows the marked attenuation in the rate of increase in the logarithmic behavior of the Jacob's working curve, so that the photoabsorber concentration can essentially be tailored for a target layer thickness to render the height insensitive to the exposure duration. For instance, 0.05 wt% of Sudan I is best suited to a layer thickness of about 25 μm , whereas 0.01 wt% Sudan I should be used for 75 μm -thick layers. Furthermore, dissolving 0.5 wt% Sudan I in an HDDA-based resin eliminated the random over-curing and flattened the surfaces as shown in Fig. 4g, but the same absorber roughened the optically-clear surface of the HDDMA-based solution (Fig. 4h). The latter was due to the much lower curing depth of the di(meth)acrylate compared to diacrylate resin, which limited solidification to central regions of pixels (Fig. 4i), producing the peaks present in the resulting surface. Altering the absorber to Rhodamine B or DODCI in PEGDA(700)-based solutions resulted in no effect on feature shape, or surface roughness using Rhodamine B and rugged surfaces with DODCI.

The role of a secondary monomer/oligomer; i.e. 'crosslinker', is examined by combining 0.5 vol fraction of all combinations of the mono, di, di(meth), and tri-acrylates, with and without the Sudan I photoabsorber, as denoted by solutions #21-30 in Table 1. As in Fig. 4f, the PPGA-TETA and HDDA-HDDMA combinations had the highest and lowest curing depths, respectively, where the PPGA-TETA cured about 7.2 times faster for a 10 s exposure. Among the hybrid resins, PPGA-HDDA and HDDA-TETA solutions produced uniform layer surfaces, but the PPGA-HDDMA and HDDA-HDDMA resins yielded the best surface quality (Fig. 4j). All hybrid resins containing 0.1 wt% of Sudan I absorber (i) underwent a significant reduction in curing depth (e.g. approximately 6-fold for PPGA-TETA), (ii) significantly reduced the rate of increase in the logarithmic behavior of the Jacob's curve, and (iii) had flat, relatively smooth surfaces with nearly identical topography. Indeed, use of hybrid combinations of monomers/oligomers also influenced their rheological properties (Table 1), hence hybrid resin formulation could be strategically used to tailor viscosity ($\eta = 0.01\text{--}0.19\text{ Pa}\cdot\text{s}$).

3.3. Optimally-devised formulations and implications

The following novel conclusions are drawn from the evidence provided by the findings of the present work, which can be taken as directions for the formulation of resins to provide maximum resolution, the highest surface quality, and minimal 'stair-stepping' layering artifacts for DLP-based microstereolithographic 3D printing:

- 1 Single-pixel projections could produce conical and aspherical features with smooth walls a fraction of the size of a pixel. Controlled-fabrication of such features at the near-nanoscale in a non-layered manner is currently limited to the use of two-photon laser writing

[28] and has not been achieved using the DLP-based technique that is relatively rapid. Such geometries hold promising implications in various applications such as micro-optics fabrication and in microfluidics where they can facilitate direct printing of functional superhydrophobic surfaces on micro-channel surfaces [13] or be used to fabricate waveguide devices used in acoustofluidic particle manipulation applications [43].

- 2 Surfaces (i.e. layers) of optical surface quality could be produced exclusively using the di(meth)acrylate-based resin (HDDMA, solution #7) that contained no photoabsorber additive. Fig. 5d compares the opacity of the di(methacrylate)-based solution to a diacrylate-based resin and shows the relatively rough surface produced by the diacrylate resin (surface topography in Fig. 4c) under otherwise identical conditions. This finding enables the use of this formulation in the fabrication of micro-optical elements using a DLP-based maskless soft lithography approach [44], which remains as the topic for a complementary study.
- 3 On account of smooth surface fabrication above, we demonstrate that solution #7 employed in a layer-by-layer fabrication could significantly reduce the 'stair-stepping' layering artifact that remains at the core of all layered additive manufacturing processes. Fig. 5e shows an array of microlenses fabricated using a layer thickness of 4 μm which, compared to a diacrylate-based lens in Fig. 5f, has a smooth surface with almost no stair-stepping. Fig. 5g shows that a micro-lattice structure with smooth, transparent beams was fabricated using solution #7.
- 4 Use of a suitable photoabsorber enables printing of structures having individual layers of less than 4 μm , the maximum vertical resolution obtained using our DLP-based system. Moreover, the thinnest single-pixel-wide line we fabricated had a width of less than 7 μm , shown in Fig. 5a.
- 5 Monomer/oligomer functional group had the most profound effect on resolution, sidewall slope, and surface uniformity and smoothness and were insensitive to the backbone type; e.g. diacrylate-based HDDA and PEGDA solutions with comparable M_w produced similarly-shaped micro-features and surface topographies, whereas monoacrylate, dimethacrylate, or triacrylate-based resins yielded different single-pixel micro-feature shapes, surface topographies, and sidewall angles (Fig. 4).

4. Conclusions

The relationship between photocurable polymer resin formulation and the resulting resolution and quality of features fabricated was experimentally explored using a recently-developed high-resolution, bottom-exposure, multimaterial, DLP-based 3D printing system. Micro-features forming due to single-pixels, single-pixel-wide lines, and multi-pixel surface projections for various light exposure times provided a basis for comparative analyses of feature shape, size, and surface quality, between resins of varying constituent types and concentrations. The interplay of pre-polymer constituents, namely mono, di, di(meth), and tri-functional acrylate oligomers, photoinitiator systems, and photoabsorbers was observed to strongly govern printed feature properties.

We found that sub-pixel conical and aspherical features with smooth walls could be fabricated using single-pixel projections. The shape and size of these features could be precisely and repeatedly controlled by varying resin formulation and process parameters with implications in micro-optic and microfluidic fabrication. We devised optimized resins and demonstrated that a di(meth)acrylate-based solution produced optically-clear layers in contrast to opaque surfaces resulting from diacrylate-based resins. Moreover, the use of this solution minimized the 'stair-stepping' effect in components printed in a layer-by-layer manner. We also showed that the maximum lateral and vertical resolution attainable using our present system were 7 μm and 4 μm , respectively, while maintaining uniform width and height. The process-control framework established here is aimed to serve as a guide for the

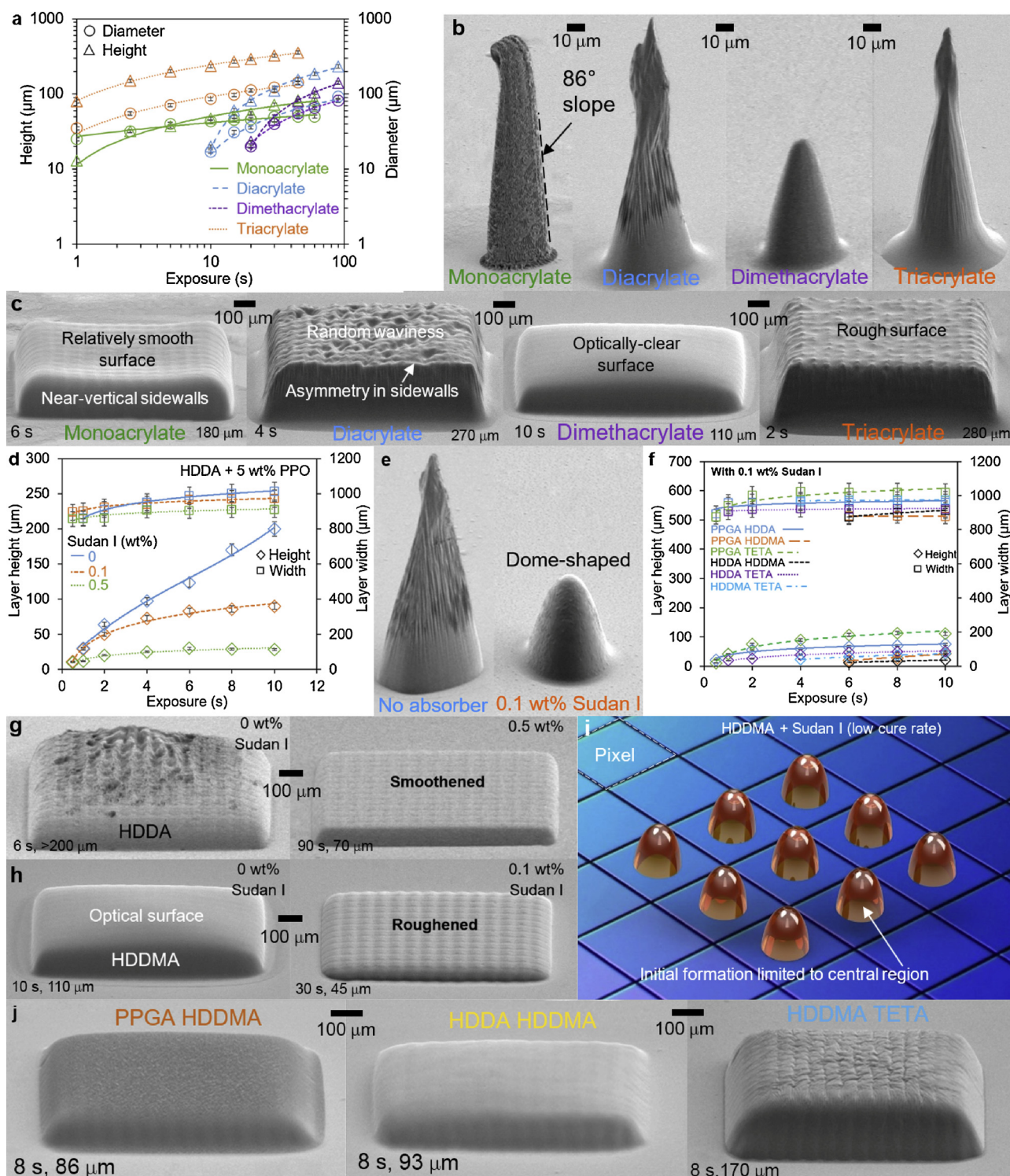


Fig. 4. Effects of functional group, absorbers, and crosslinkers (solutions #1, 6–8, 13–20, 21–30). Plots of single-pixel and layer dimensions versus exposure for (a) various monomer/oligomer functional groups, (d) photoabsorber concentrations, (f) various crosslinkers. Isometric SEM views of single-pixel and 15 px × 15 px surfaces for (b and c) various monomer/oligomer functional groups, (e, g, and h) photoabsorber concentrations, (j) various crosslinkers.

open-source design of photocurable polymers that conform to the highest resolution and quality for a given pixel size over a versatile range of mechanical properties.

Acknowledgements

The authors gratefully acknowledge support from SUTD Digital

Manufacturing and Design Centre (DManD) funded by the Singapore National Research Foundation. Q.G. acknowledges SUTD Start-up Research Grant. The authors thank the help and guidance of Professor Robert E. Simpson at SUTD on refractive index measurement.

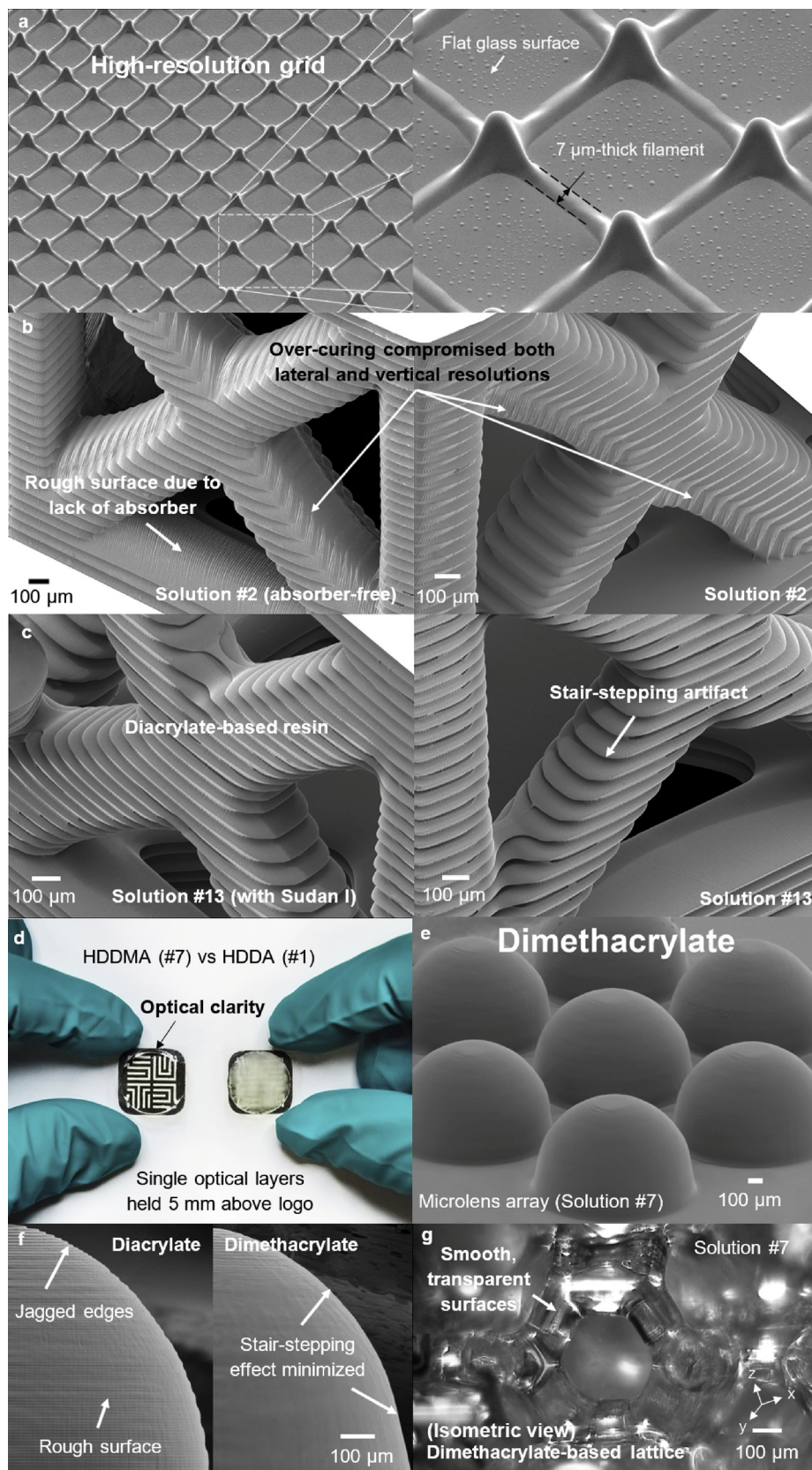


Fig. 5. Components fabricated utilizing optimally-devised resins. (a) SEM images of a high-resolution grid containing 7 μm-wide filaments. Exposure: 0.25 s using solution #1. (c) Close-up SEM images of lattice structures fabricated using diacrylate-based solutions #2 and #13 (exposures of 0.5 and 5 s, respectively) with and without Sudan I. (d) Optically-clear single layers made using solutions #7 and #1 (exposures of 5 and 2 s, respectively). (e–f) Microlenses fabricated using diacrylate- and di(meth)acrylate-based resins (solutions #2 and #7, exposures of 0.5 and 2 s, respectively). (g) Microscope image showing the transparency of beams within a lattice fabricated using solution #7 (layer thickness: exposure: 2 s).

Table 3
List of reflectance at 405 nm of the cured films made of different photopolymer formulations.

HDDA, 226	HDDMA, 254	PEGDA, 250	PEGDA, 575	PEGDA, 700	TETA, 146
4.52%	4.32%	4.64%	4.42%	4.39%	4.9%

Appendix A. Refractive index measurement

We measured the reflectance of solidified photopolymer films on a spectrophotometer (LAMBDA™ 750 UV/Vis/NIR PerkinElmer, MA, USA). The spectra from 320 nm to 800 nm were scanned at a rate of 266.75 nm/min. The tested photopolymer films were prepared by sandwiching the liquid resin in the middle of two glass slides followed by a 10-minute exposure in a UV oven (365 nm, CL-1000 Ultraviolet crosslinker, USA). The thickness of the resulting films was 1.1 mm.

The refractive index of the cured film was calculated by Fresnel equation as follows:

$$R = \left| \frac{n_a - n_f}{n_a + n_f} \right|^2, \quad (2)$$

where R is the power reflectance, n_a and n_f are the refractive indices of ambient air and the cured film, respectively. The value of n_a is 1. As n_f is always greater than n_a , Eq. (2) can be rewritten to

$$n_f = \frac{1 + \sqrt{R}}{1 - \sqrt{R}}. \quad (3)$$

R is obtained for the reflection spectrum at 405 nm wavelength. Table 3 lists all the reflectance at 405 nm of the cured films made of different photopolymer formulations.

References

- [1] B. Mueller, Additive manufacturing technologies—Rapid prototyping to direct digital manufacturing, *Assem. Autom.* 32 (2) (2012).
- [2] C. Barnatt, 3D printing: the next industrial revolution, *ExplainingTheFuture.com Nottingham* 2013.
- [3] M. Vaezi, H. Seitz, S. Yang, A review on 3D micro-additive manufacturing technologies, *Int. J. Adv. Manuf. Technol.* 67 (5-8) (2013) 1721–1754.
- [4] N. Guo, M.C. Leu, Additive manufacturing: technology, applications and research needs, *Front. Mech. Eng.* 8 (3) (2013) 215–243.
- [5] M.P. Lee, G.J. Cooper, T. Hinkley, G.M. Gibson, M.J. Padgett, L. Cronin, Development of a 3D printer using scanning projection stereolithography, *Sci. Rep.* 5 (2015) 9875.
- [6] Q. Ge, A.H. Sakhaei, H. Lee, C.K. Dunn, N.X. Fang, M.L. Dunn, Multimaterial 4D printing with tailorable shape memory polymers, *Sci. Rep.* 6 (2016) 31110.
- [7] X. Zheng, W. Smith, J. Jackson, B. Moran, H. Cui, D. Chen, J. Ye, N. Fang, N. Rodriguez, T. Weisgraber, Multiscale metallic metamaterials, *Nat. Mater.* 15 (10) (2016) 1100–1106.
- [8] C. Sun, N. Fang, D. Wu, X. Zhang, Projection micro-stereolithography using digital micro-mirror dynamic mask, *Sens. Actuators A Phys.* 121 (1) (2005) 113–120.
- [9] Q. Wang, J.A. Jackson, Q. Ge, J.B. Hopkins, C.M. Spadaccini, N.X. Fang, Lightweight mechanical metamaterials with tunable negative thermal expansion, *Phys. Rev. Lett.* 117 (17) (2016) 175901.
- [10] Y.Y.C. Choong, S. Maleksaedi, H. Eng, P.-C. Su, J. Wei, Curing characteristics of shape memory polymers in 3D projection and laser stereolithography, *Virtual Phys. Prototyp.* 12 (1) (2017) 77–84.
- [11] M. Shusteff, A.E. Browar, B.E. Kelly, J. Henriksson, T.H. Weisgraber, R.M. Panas, N.X. Fang, C.M. Spadaccini, One-step volumetric additive manufacturing of complex polymer structures, *Sci. Adv.* 3 (12) (2017) eaao5496.
- [12] J.R. Tumbleston, D. Shirvanyants, N. Ermoshkin, R. Janusziewicz, A.R. Johnson, D. Kelly, K. Chen, R. Pinschmidt, J.P. Rolland, A. Ermoshkin, Continuous liquid interface production of 3D objects, *Science* 347 (6228) (2015) 1349–1352.
- [13] Y. Yang, X. Li, X. Zheng, Z. Chen, Q. Zhou, Y. Chen, 3D-Printed Biomimetic Super-Hydrophobic Structure for Microdroplet Manipulation and Oil/Water Separation, *Adv. Mater.* (2017).
- [14] H. Gong, B.P. Bickham, A.T. Woolley, G.P. Nordin, Custom 3D printer and resin for $18 \mu\text{m} \times 20 \mu\text{m}$ microfluidic flow channels, *Lab Chip* 17 (17) (2017) 2899–2909.
- [15] C. Zhou, Y. Chen, Z. Yang, B. Khoshnevis, Annual solid freeform fabrication symposium, Development of Multi-Material Mask-Image-Projection-Based Stereolithography for the Fabrication of Digital Materials (2011).
- [16] J.-W. Choi, H.-C. Kim, R. Wicker, Multi-material stereolithography, *J. Mater. Process. Technol.* 211 (3) (2011) 318–328.
- [17] K. Arcaute, N. Zuverza, B. Mann, R. Wicker, Multi-material stereolithography: spatially-controlled bioactive poly (ethylene glycol) scaffolds for tissue engineering, Proceedings of 18th Annual Solid Freeform Fabrication Symposium (2007) 458–469.
- [18] R. Raman, B. Bhaduri, M. Mir, A. Shkumatov, M.K. Lee, G. Popescu, H. Kong, R. Bashir, High-Resolution Projection Microstereolithography for Patterning of Neovasculature, *Adv. Healthc. Mater.* 5 (5) (2016) 610–619.
- [19] C. Zhou, Y. Chen, Z. Yang, B. Khoshnevis, Digital material fabrication using mask-image-projection-based stereolithography, *Rapid Prototyp. J.* 19 (3) (2013) 153–165.
- [20] C. Zhou, H. Ye, F. Zhang, A novel low-cost stereolithography process based on vector scanning and mask projection for high-accuracy, high-speed, high-throughput, and large-area fabrication, *J. Comput. Inf. Sci. Eng.* 15 (1) (2015) 011003.
- [21] M.M. Emami, F. Barazandeh, F. Yaghmaei, Scanning-projection based stereolithography: Method and structure, *Sens. Actuators A Phys.* 218 (2014) 116–124.
- [22] F. Kotz, K. Arnold, W. Bauer, D. Schild, N. Keller, K. Sachsenheimer, T.M. Nargang, C. Richter, D. Helmer, B.E. Rapp, Three-dimensional printing of transparent fused silica glass, *Nature* 544 (7650) (2017) 337.
- [23] X. Zheng, H. Lee, T.H. Weisgraber, M. Shusteff, J. DeOtte, E.B. Duoss, J.D. Kuntz, M.M. Biener, Q. Ge, J.A. Jackson, Ultralight, ultrastiff mechanical metamaterials, *Science* 344 (6190) (2014) 1373–1377.
- [24] Y. Pan, X. Zhao, C. Zhou, Y. Chen, Smooth surface fabrication in mask projection based stereolithography, *J. Manuf. Process.* 14 (4) (2012) 460–470.
- [25] K. Kowsari, S. Akbari, D. Wang, N.X. Fang, Q. Ge, High-Efficiency, High-Resolution Multimaterial Fabrication for Digital Light Processing Based Three-Dimensional Printing, *3D Print. Addit. Manuf.* 5 (3) (2018) 185–193.
- [26] Y. Pan, C. Dagli, Dynamic resolution control in a laser projection-based stereolithography system, *Rapid Prototyp. J.* 23 (1) (2017) 190–200.
- [27] C. Zhou, Y. Chen, Additive manufacturing based on optimized mask video projection for improved accuracy and resolution, *J. Manuf. Process.* 14 (2) (2012) 107–118.
- [28] L. Nguyen, M. Straub, M. Gu, Acrylate-based photopolymer for two-photon microfabrication and photonic applications, *Adv. Funct. Mater.* 15 (2) (2005) 209–216.
- [29] M.M. Zabt, Effects of Light Absorber on Micro Stereolithography Parts, University of Birmingham, 2012.
- [30] B.D. Fairbanks, M.P. Schwartz, C.N. Bowman, K.S. Anseth, Photoinitiated polymerization of PEG-diacrylate with lithium phenyl-2, 4, 6-trimethylbenzoylphosphinate: polymerization rate and cytocompatibility, *Biomaterials* 30 (35) (2009) 6702–6707.
- [31] H. Gong, M. Beauchamp, S. Perry, A.T. Woolley, G.P. Nordin, Optical approach to resin formulation for 3D printed microfluidics, *RSC Adv.* 5 (129) (2015) 106621–106632.
- [32] J. Stampfl, S. Baudis, C. Heller, R. Liska, A. Neumeister, R. Kling, A. Ostendorf, M. Spitzbart, Photopolymers with tunable mechanical properties processed by laser-based high-resolution stereolithography, *J. Micromech. Microeng.* 18 (12) (2008) 125014.
- [33] A. Au, A. Gonzalez-Suarez, U. Nallapati, N. Bhattacharjee, A. Karkamkar, C. De Forest, J. Garcia-Cordero, A. Folch, Biocompatible 3D-printed peg-diacrylate microfluidics, 19th International Conference on Miniaturized Systems for Chemistry and Life Sciences (2015).
- [34] J. Tobia, Development and Characterization of a Droplet-Based Material Feed System for Multi-Material Projection Micro-stereolithography, Rutgers The State University of New Jersey-New Brunswick, 2016.
- [35] V. Chan, J.H. Jeong, P. Bajaj, M. Collens, T. Saif, H. Kong, R. Bashir, Multi-material bio-fabrication of hydrogel cantilevers and actuators with stereolithography, *Lab Chip* 12 (1) (2012) 88–98.
- [36] S.W. Benson, A.M. North, The kinetics of free radical polymerization under conditions of diffusion-controlled termination, *J. Am. Chem. Soc.* 84 (6) (1962)

- 935–940.
- [37] I. Gibson, D.W. Rosen, B. Stucker, *Design for Additive Manufacturing*, Additive Manufacturing Technologies, Springer, 2010, pp. 299–332.
- [38] J. Dominguez, M. Alonso, M. Oliet, F. Rodriguez, Chemorheological study of the curing kinetics of a phenolic resol resin gelled, *Eur. Polym. J.* 46 (1) (2010) 50–57.
- [39] P.F. Jacobs, *Rapid Prototyping & Manufacturing: Fundamentals of Stereolithography*, Society of Manufacturing Engineers, 1992.
- [40] H. Lipson, M. Kurman, *Fabricated: The New World of 3D Printing*, John Wiley & Sons, 2013.
- [41] A.S. Kewitsch, A. Yariv, Self-focusing and self-trapping of optical beams upon photopolymerization, *Opt. Lett.* 21 (1) (1996) 24–26.
- [42] J. Zhang, K. Saravanamuttu, The dynamics of self-trapped beams of incoherent white light in a free-radical photopolymerizable medium, *J. Am. Chem. Soc.* 128 (46) (2006) 14913–14923.
- [43] D.J. Collins, R. O'Rourke, C. Devendran, Z. Ma, J. Han, A. Neild, Y. Ai, Self-Aligned Acoustofluidic Particle Focusing and Patterning in Microfluidic Channels from Channel-Based Acoustic Waveguides, *Phys. Rev. Lett.* 120 (7) (2018) 074502.
- [44] K. Totsu, K. Fujishiro, S. Tanaka, M. Esashi, Fabrication of three-dimensional microstructure using maskless gray-scale lithography, *Sens. Actuators A Phys.* 130 (2006) 387–392.